Hindawi
International Journal of Antennas and Propagation
Volume 2019, Article ID 6956809, 13 pages
https://doi.org/10.1155/2019/6956809

Research Article

Imaging Internal Defects with Synthetic and Experimental Data

Hongwei Zhou,[1] Guanghui Hu,[2] and Ling Ma [1]

[1]*Northeast Forestry University, Harbin 150040, China*
[2]*Beijing Computational Science Research Center, Beijing 100193, China*

Correspondence should be addressed to Ling Ma; maling63@163.com

Received 29 March 2019; Accepted 19 June 2019; Published 14 July 2019

Guest Editor: Lulu Wang

This work concerns an inverse time-dependent electromagnetic scattering problem of imaging internal defects in a homogeneous isotropic medium. The position and cross section of the defects are detected by transient electromagnetic pulses in the case of TE polarization. We apply the Kirchhoff migration scheme to locate the position of small objects from both synthetic and experimental data. The multiple-input-multiple-out scheme is used to recover extended scatterers from the data generated by the software GprMax. Numerical experiments show that the Kirchhoff migration method is not only efficient but also robust with respect to polluted data at high noise levels. Experimental results show good quantitative agreement with numerical simulations.

1. Introduction

Inverse scattering is to recover physical and geometrical information of inaccessible objects from scattered fields measured outside. It has been one of the most challenging problems with considerable practical applications in many areas of technology such as nondestructive evaluation, subsurface and ground-penetrating radar, geophysical remote sensing, medical imaging, seismology, and target identification; see [1–5]. One of the most prominent features of inverse scattering problem is its noninvasiveness, along with the affordability due to cheap nonionizing sensors. However, solving inverse scattering problems is difficult due to the inherent ill-posedness and nonlinearity. Small variation in the measured data can lead to large errors in the reconstruction of the scatterer, unless regularization methods are used. Extensive investigation has been carried out and a variety of inversion algorithms have been proposed.

In the time-harmonic regime, Kirsch and Kress [6, 7], Colton and Monk [8, 9], and Angrll, Kleiman, and Roach [10] theoretically separate the nonlinearity and the ill-posedness of inverse obstacle problems, giving rise to the decomposition method. Saqib et al. [11], Yang et al. [12], and Gan et al. [13] employed iterative methods to solve inverse obstacle problems. In these optimization-based iterative approaches, an efficient forward solver is needed for each iteration, and good a priori information might be required in order to choose an initial guess that ensures numerical convergence. Noniterative sampling methods were intensively studied over the last twenty years, for instance, linear sampling method [14], factorization method [15], enclosure method [16], and singular point source method [17]. The key ingredient of the sampling approach is to design an appropriate indicator function from measured data for characterizing the region occupied by the scatterer. Forward solvers are not needed in the process of inversion. The above-mentioned approaches are mostly applicable to measured data irradiated at a fixed energy with many incoming directions. A recursive linearization method with multifrequency data was investigated in [18–22].

There exist a number of reconstruction algorithms in the time domain with dynamic measurement data. Here we mention the time reversal techniques [23, 24], the reversed time migration [25], and the boundary control method [26]. For time-dependent sampling type methods, we refer to the point source method [27], the enclosure method [28], and the total focusing method (TFM) arising from nondestructive evaluation [29, 30]. In one of the author's previous works [31], the TFM (which is also known as the Kirchhoff migration approach used in geophysics; see, e.g., [32]) was examined for imaging acoustically extended scatterers in two dimensions and the indicator behavior was mathematically analyzed. This

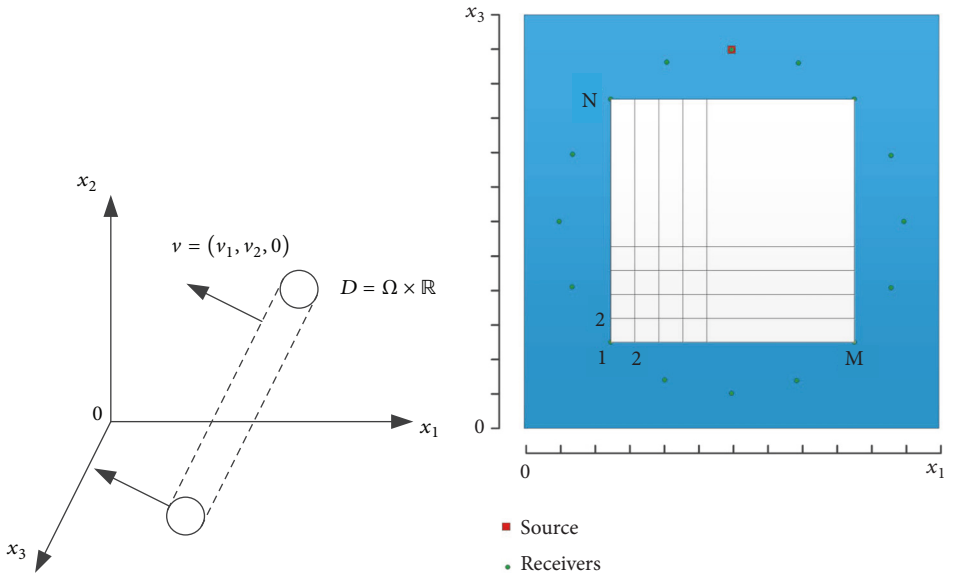

(a) Geometrical model (b) Sample grid subdivision

Figure 1: Geometrical schematic.

work concerns imaging internal defects in a homogeneous isotropic medium. It is shown that the TFM is not only efficient but also robust to measurement noise. The aim of this paper is to test the TFM for inverse electromagnetic scattering problem of imaging perfectly conducting cylinders buried in a half-space homogeneous isotropic background medium. Such kind of inverse problems has many applications in searching for internal defects with radar techniques like ground-penetrating radar (GPR); see, e.g., [5, 33, 34]. We note that the light speed is much faster than the sound speed, leading to additional difficulties in computational simulation [35]. In this paper, we make use of the open software GprMax [35, 36] to generate the forward scattering data. The GprMax is an electromagnetic simulation tool based on the Finite-Difference Time-Domain (FDTD) approach coupled with the perfectly matched layer (PML) technique. In our experiments, the real data are gained by GPR.

In this paper, we apply the TFM (or Kirchhoff migration scheme) to inverse electromagnetic scattering problems. In comparison to other algorithms, the implementation of TFM is quite simple, since the image is formed through a superposition of the scattered signals irradiated by each transducer. In fact, our imaging functions are explicit and involve only integral calculations on the measurement surface. Hence, our inversion algorithm is totally "direct". This also explains why this method is very robust with respect to measurement noise at high levels. Although the inverse scattering problem is difficult due to the inherent ill-posedness and nonlinearity, we do not need to solve the ill-posed and nonlinear problems, even without approximation and iteration. In this work, experiments with synthetic and experimental data are conducted to demonstrate the feasibility and applicability of this approach in the TE polarization case of inverse electromagnetic scattering problems.

The remaining part of this paper is organized as follows. In Section 2 we rigorously formulate the forward and inverse electromagnetic scattering problems. Section 3 is devoted to the description and implementation of the TFM for imaging small scatterers from both synthetic and real data. Extended scatterers will be reconstructed in Section 4 by using GprMax simulated data. Conclusion follows in Section 5.

2. Problem Setting

Consider the electromagnetic wave propagation in a homogeneous isotropic medium. This background medium can be characterized by the electric permittivity ε, magnetic permeability μ, and electric conductivity σ, all of which are assumed to be constant. The propagation of the electric and magnetic fields (E, H) is governed by the Maxwell system.

$$\operatorname{curl} E + \mu \frac{\partial H}{\partial t} = 0 \tag{1}$$

$$\operatorname{curl} H - \varepsilon \frac{\partial E}{\partial t} = \sigma E \tag{2}$$

Assume that $D = \Omega \times \mathbb{R}$ is an infinitely long perfectly conducting cylinder buried in the lower half-space $x_2 < 0$, which remains invariant in x_3-direction; see Figure 1(a). The medium in the exterior $D^e := \mathbb{R}^3 \setminus \overline{D}$ of D is assumed to be dielectric, which means that $\sigma = 0$. The cross section of D in the ox_1x_2-plane is denoted by $\Omega \subset \mathbb{R}^2_- := \{x = (x_1, x_2) : x_2 < 0\}$. Incident cylindrical source waves emitted from the surface $\Gamma \subset (\mathbb{R}^3 \setminus \overline{D}) \cap \{x_3 = 0\}$ will be utilized for the purpose of detecting the position and shape of Ω. Throughout the paper, we assume that the incident wave $E^i_\chi(\mathrm{x}, t; \mathrm{y})$ with $\mathrm{x} = (x, x_3)$, $\mathrm{y} = (y, y_3) \in \mathbb{R}^3$, $t > 0$ is a filamentary current

generated at the source location $y \in \Gamma$ with a temporal pulse signal $\chi : \mathbb{R} \longrightarrow \mathbb{R}$. The temporal function is supposed to have a compact support $(\chi)(t) \in (0, T_0)$ for some $T_0 > 0$. Moreover, we consider the Transverse Electric (TE) case of the monopole with the polarization direction $e_3 = (0, 0, 1)$. Then, the incident electric and magnetic waves (E^i, H^i) are governed by the system

$$\begin{aligned} \operatorname{curl} E^i(\mathrm{x}, t; \mathrm{y}) + \mu \frac{\partial H^i(\mathrm{x}, t; \mathrm{y})}{\partial t} &= 0 \\ \operatorname{curl} H^i(\mathrm{x}, t; \mathrm{y}) - \varepsilon \frac{\partial E^i(\mathrm{x}, t; \mathrm{y})}{\partial t} &= -\delta(\mathrm{x} - \mathrm{y}) \chi(t) e_3 \end{aligned} \tag{3}$$

for all $\mathrm{x} \neq \mathrm{y}$, $\mathrm{x} \in D^e$, and $t > 0$, where δ is the Dirac distribution. Denote by (E^s, H^s) the scattered fields and write the total field as $E = E^i + E^s$, $H = H^i + H^s$. Then, we have

$$\begin{aligned} \operatorname{curl} E(\mathrm{x}, t; \mathrm{y}) + \mu \frac{\partial H(\mathrm{x}, t; \mathrm{y})}{\partial t} &= 0 \quad \text{in } D^e \setminus \{\mathrm{y}\} \times \mathbb{R}_+, \\ \operatorname{curl} H(\mathrm{x}, t; \mathrm{y}) - \varepsilon \frac{\partial E(\mathrm{x}, t; \mathrm{y})}{\partial t} &= -\delta(\mathrm{x} - \mathrm{y}) \chi(t) e_3 \quad \text{in } D^e \setminus \{\mathrm{y}\} \times \mathbb{R}_+, \\ \nu \times E(\mathrm{x}, t; \mathrm{y}) &= 0 \quad \text{on } \partial D \times \mathbb{R}_+, \end{aligned} \tag{4}$$

together with the zero initial condition at $t = 0$ in $\mathbb{R}^3$. Here $\nu = (\nu_1, \nu_2, \nu_3)$ is the unit outward normal to the boundary ∂D. Eliminating the magnetic field, we arrive at

$$\begin{aligned} \frac{\partial^2 E(\mathrm{x}, t; \mathrm{y})}{\partial t^2} = &-\frac{1}{\varepsilon\mu} \operatorname{curl} \operatorname{curl} E(\mathrm{x}, t; \mathrm{y}) \\ &+ \frac{1}{\varepsilon} \delta(\mathrm{x} - \mathrm{y}) \partial_t \chi(t) e_3, \quad \mathrm{x} \neq \mathrm{y}. \end{aligned} \tag{5}$$

In the TM polarization case, the electric field takes the form $E(\mathrm{x}) = (0, 0, u(x))$. Hence, the perfectly conducting boundary condition can be written as

$$\nu \times E = \begin{bmatrix} i & j & k \\ \nu_1 & \nu_2 & 0 \\ 0 & 0 & u \end{bmatrix} = (\nu_2 u, -\nu_1 u, 0) \quad \text{on } \partial D \times \mathbb{R}_+, \tag{6}$$

implying that $u = 0$ on $\partial D \times \mathbb{R}_+$. Using

$$\operatorname{curl} \operatorname{curl} E(\mathrm{x}) = -\Delta E(\mathrm{x}) + \operatorname{grad} \operatorname{div} E(\mathrm{x}), \tag{7}$$

we deduce the reduced wave equation from the Maxwell system (5) as follows:

$$\begin{aligned} \frac{\partial^2 u(\mathrm{x}, t; \mathrm{y})}{\partial t^2} = \frac{1}{\varepsilon\mu} \Delta u(\mathrm{x}, t; \mathrm{y}) + \frac{1}{\varepsilon} \delta(\mathrm{x} - \mathrm{y}) \partial_t \chi(t), \\ \mathrm{x} \in \mathbb{R}^2 \setminus \left\{ \overline{\Omega} \cup \{\mathrm{y}\} \right\} \times \mathbb{R}_+. \end{aligned} \tag{8}$$

In the particular case that $\chi(t) = \sin(\omega t)$ is a 2π-periodic function, where ω denotes the frequency, the incident field u^{in} can be explicitly represented as

$$u^{in}(\mathrm{x}, t; \mathrm{y}) = \mu\omega \mathrm{Re} \left\{ \frac{i}{4} H_0^{(1)} \left(\frac{\omega}{c} |\mathrm{x} - \mathrm{y}| \right) e^{i\omega t} \right\}, \quad \mathrm{x} \neq \mathrm{y}. \tag{9}$$

Here $H_0^{(1)}$ is the Hankel function of first kind of order zero; see [37, Chapter 3.4].

In this paper we shall consider the following inverse problem:

> (IP): determine the position and shape of $\partial\Omega$ from knowledge of $u^s(x, t; y)$ irradiated by incident dipoles located at $y \in \Gamma$.

Throughout this paper, we use the temporal function of the form

$$\chi(t) = -A \left[2\pi^2 f^2 \left(t - \frac{\sqrt{2}}{f} \right)^2 - 1 \right] e^{-\pi^2 f^2 (t - \sqrt{2}/f)^2}, \quad t > 0, \tag{10}$$

which is known as the Ricker pulse. Here $f > 0$ is the center frequency and $A > 0$ 0 is the amplitude. The incident pulse function $\chi(t)$ with $f = 6$ GHz is depicted in Figure 2.

We shall consider two cases:

(i) $\Omega \in \mathbb{R}^2_-$ is a small object (compared to the incident wavelength), $\Gamma = \{(x_1, b) : a_1 < x_1 < a_2\}$ is a finite line segment, and the data are given by $\{u^s(x, t; x)\}$ for all $(x, t) \in \Gamma \times (0, T)$.

(ii) Ω is an extended scatterer, $\Gamma = \{x \in \mathbb{R}^2 : |x| = R\}$ for some $R > 0$ such that $\Omega \subset B_R := \{x \in \mathbb{R}^2 : |x| < R\}$, and the data are given by $\{u^s(\mathrm{x}, t; \mathrm{y})\}$ for all $(\mathrm{x}, t) \in \Gamma \times (0, T)$ irradiated by many dipoles emitted from Γ.

Note that in case (i), the positions of the receivers and transmitters are identical, leading to the so-called inverse back scattering problem, whereas the case (ii) corresponds to a multiple-input-multiple-output (MIMO) radar system. The aim of this paper is to apply the total focusing method to the above inverse electromagnetic scattering problems with synthetic and experimental data. The TFM is sometimes described as the "gold standard" in the classical beamforming. Both TFM and the Kirchhoff migration form the image with the superposition of the scattered signals irradiated by each transmitter.

3. Imaging Small Scatterers

In this section we suppose that a single metal stick is buried in sand below the ground plane $\{x_2 = b\}$. The cross section Ω of the metal is so small compared to the wavelength such that Ω can be regarded as a point-like object. The electric dipoles are generated on part of the ground plane $\Gamma = \{(x_1, b) : a_1 < x_1 < a_2\}$ for some $a_j > 0$ $(j = 1, 2)$. The Kirchhoff migration imaging scheme for inverse back scattering consists of the following three steps:

Firstly, we take the searching area as a rectangular domain in the lower half-space $\mathbb{R}^2_-$ and divide it into an $M \times N$ grid. The grid points, as shown in Figure 1(b), will be referred to as sampling points $z \in \mathbb{R}^2_-$. We shall design an imaging function defined on these grid points.

Secondly, the filamentary current is transmitted from the source position $\{x^{(k)} = (k(a_2 - a_1)/N, 0)\}$ and the scattered signals are also recorded at the same position $x^{(k)}$, which we

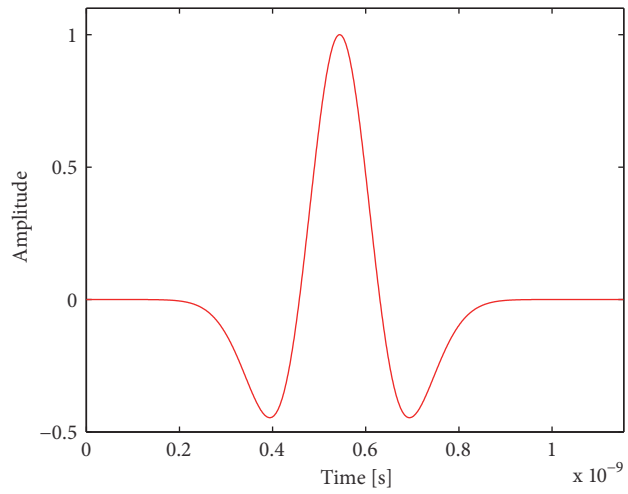

FIGURE 2: The Ricker pulse with $f = 6$ GHz and $A = 1$.

denote by $u_k^s(t) := u^s(x^{(k)}, t; x^{(k)})$ for $k = 1, 2, \ldots, N$. Note that $u^s(x, t; y) = u(x, t; y) - u^i(x, t; y)$ stands for the scattered wave field. Calculate the flight time of the signal emitted from $x^{(k)}$ to a sampling point z and then returned back to the receiver $x^{(k)}$, given by

$$t_k(z) = \frac{2\left|x^{(k)} - z\right|}{c}, \quad k = 1, 2, \ldots, N. \tag{11}$$

Here $c = \sqrt{1/(\varepsilon\mu)} > 0$ denotes the light speed in the background medium. In particular, we have $c = c_0\sqrt{\varepsilon}$ in terms of the light speed c_0 in the vacuum.

Thirdly, collect all signals u_k^s for $k = 1, 2, \ldots, N$ and plot the indicator function

$$I(z) = \left|\sum_{k=1}^{N} u_k^s\left(t_k(z)\right)\right|^2 > 0. \tag{12}$$

Here we have assumed that the terminal T is large enough. By the mathematical analysis performed in [21], the local maximizers of I can represent the location of the small scatterer.

3.1. Imaging with Synthetic Data. To implement the Kirchhoff migration scheme, we assume that the interface between the air and the sand is given by $\{(x_1, b) : x_1 \in \mathbb{R}\}$ with $= -0.1$. The dielectric properties of the sand are considered as 4. We choose $N = 41$ receivers and transmitters uniformly lying between $(0.1, -0.1)$ and $(0.1, -0.3)$. The cross section of the metal stick is supposed to be the circle of radius 0.009 centered at $(0.2, -0.167)$; see Figure 3 for the locations of the metal stick in the ox_1x_2-plane and the first transmitter (receiver). The center frequency of Ricker waves is uniformly taken as $f = 2.6$ GHz and the amplitude is set to be $A = 1$. The terminal time is taken as

$$T = \frac{2h}{c} + \frac{1}{f}, \tag{13}$$

where $h > 0$ denotes the travel distance of the radar. In our simulations we take $T = 7 \times 10^{-9} s$.

The scattered data were generated by GprMax based on the FDTD method (see [20, 38]). The unbounded exterior domain is truncated by an absorbing boundary condition. The mesh of the forward solver is successively refined until the relative error of the successive measured scattered data is below 0.1%.

For the k-th transmitter, the scattered data u_k^s are recorded at 1063 time points given by

$$t_k = \frac{k}{1063}T, \quad k = 1, 2, \ldots, 1063. \tag{14}$$

Linear interpolation is adopted to obtain the value of $u_k^s(t)$ for an arbitrary $t \in (0, T)$. In Figure 4, we show the signals of the incident electric field and the total fields irradiated by the first transmitter. The incident field obviously has a launch waveform, as shown in Figure 4(a). The significant changes before 0.2ns are due to the transmitter itself rather than the reflected wave field from the metal stick. In Figure 4(b), one can observe the changes of the signal at about 0.4ns caused by the presence of the object. Subtracting the incident field from the total field, one can obtain the scattered signal, which will be utilized to locate the position of the stick.

For $x = (x_1, x_2) \in \mathbb{R}^2$ with $x_1 \in [0.1 + kh, 0.1 + (k+1)h]$, $h = (a_2 - a_1)/N = 0.2/268$, we first plot the function

$$B(x) := u_k^s\left(\frac{2\left|x_2 - 0.1\right|}{c}\right), \quad -0.4 < x_2 < -0.1, \tag{15}$$

which forms the B-scan image of the object. Note that only the information of the signal of u_k^s is involved in B-scan for $x_1 \in [0.1 + kh, 0.1 + (k+1)h]$, whereas all signals are required in our indicator equation (15). Figure 5(a) shows the B-scan image of the small object located at (0.2, 0.167). The x_1-coordinate of the location corresponds to the trace number 100. In Figure 5(b), one can see an approximate location of the target using our indicator (15). Numerical experiments show that the Kirchhoff migration method is not only efficient but

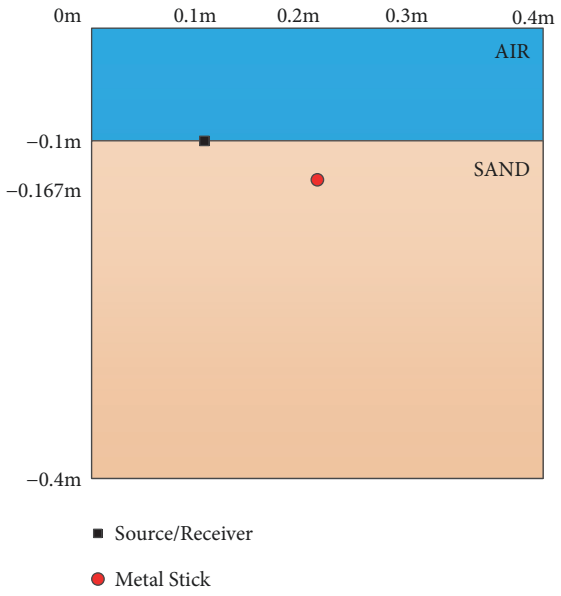

Figure 3: Locations of the first transmitter/receiver and the target.

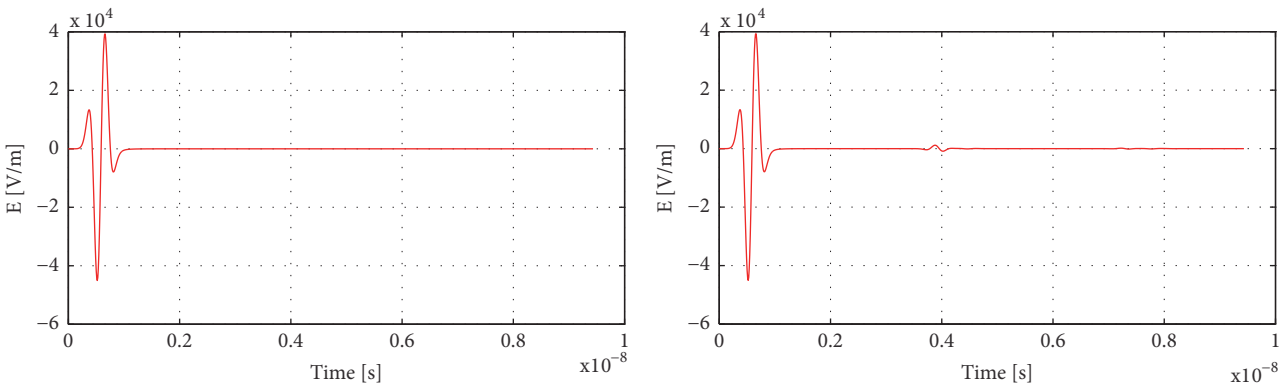

(a) Incident field (b) Total field

Figure 4: Electric signals generated by the first transmitter.

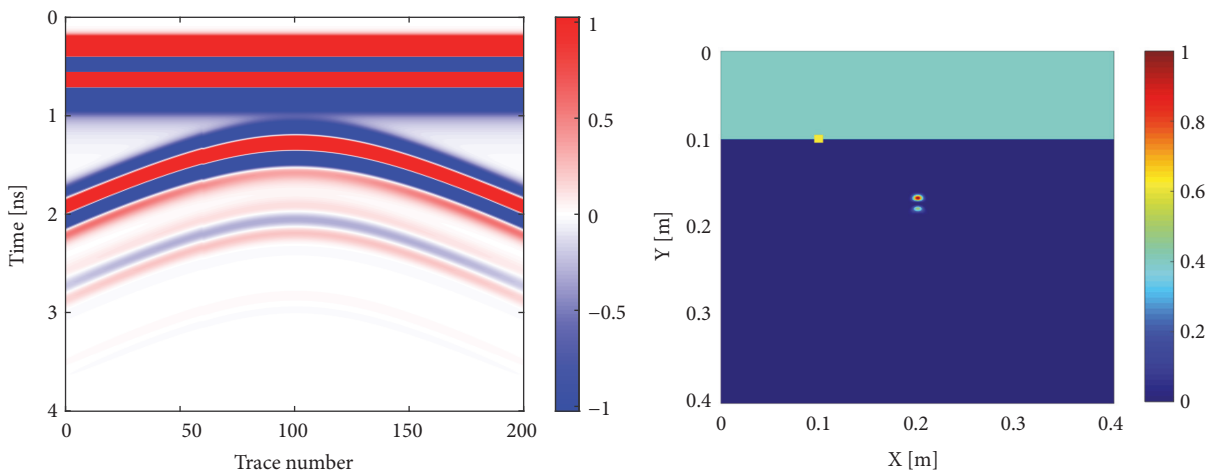

(a) B-scan image formed by the indicator equation (15) (b) The Kirchhoff migration image

Figure 5: Imaging a small scatterer using synthetic data without noise.

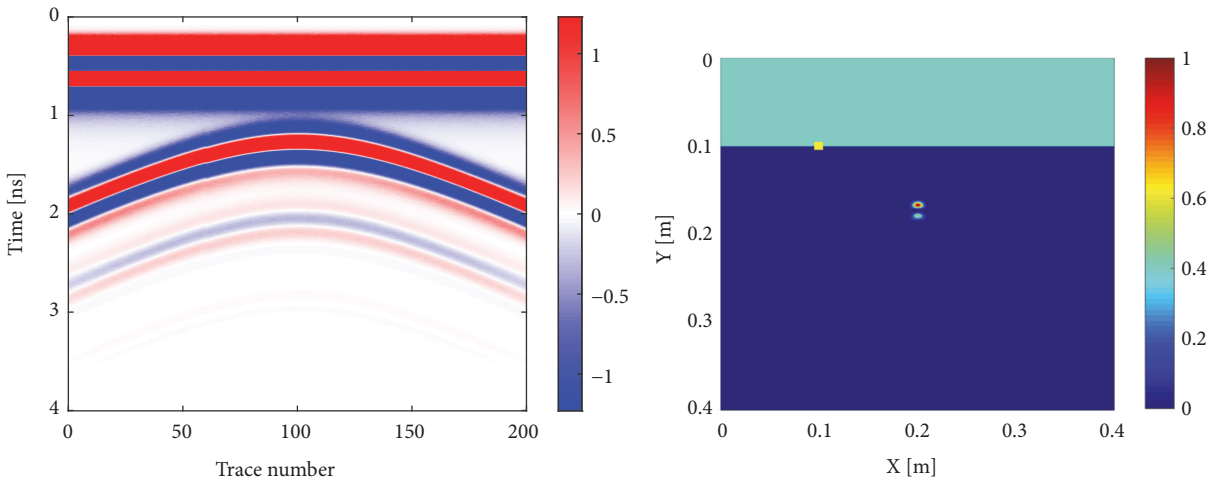

(a) B-scan image formed by the indicator equation (15)

(b) The Kirchhoff migration image

Figure 6: Imaging a small scatterer using polluted synthetic data at the noise level $\delta = 100\%$.

Figure 7: Experiment site.

also robust with respect to polluted data at high noise levels (Figure 6). Note that in this paper the scattered near-field data is polluted by

$$u_\delta^{sc}(x,t) = u^{sc}(x,t) + \delta\zeta u^{sc}(x,t), \tag{16}$$

where δ is the noise ratio and ζ is the standard normal distribution.

3.2. Imaging with Experimental Data. In our experiment settings, a metal stick is detected in a sand box by a GSSI Mini HR hand-held ground-penetrating radar; see Figure 7 for the experiment site. The size of the sand box is 0.45 m×0.3m×0.2m, the thickness of the wooden shell is 0.015m, the dielectric properties of the sand are 4, and the dielectric properties of the wooden box are considered approximately the same as the sand. For electric dipoles with TE polarization, the three-dimensional Maxwell equation can be reduced to a two-dimensional model for scalar wave equations. We set up a two-dimensional coordinate system and take the initial position of the source and receiver of the radar at (0.1, 0.1). The metal stick is centered at (0.2, 0.167) with the radius 0.009. The radar rolls along the straight line $x_2 = 0.1$ on the wooden shell and moves forward in the positive x_1-direction at an even pace. In this process there are totally 268 electric dipoles excited by the radar before it reaches the ending point (0.25, 0.1). The temporal function of the incident wave is a Ricker wavelet excited at the frequency 2.6GHz with the amplitude 1.

The B-scan image formed by our experimental data is plotted with Matlab R2013b, as shown in Figure 8(a). Figure 8(b) shows the image using the indicator (12), where the position of the target is precisely located. In comparison with the counterpart from synthetic data (see Figure 5(b)), we find that the inversion of the depth of the stick contains relatively large errors.

Next, we want to find two metal sticks with different positions. The centers of the cross section in the ox_1x_2-plane are given by (0.15, 0.15) and (0.25, 0.17), respectively. The other parameters in our experiment are the same as before. See Figure 9(b) for the experiment site and Figure 9(a) for the location of the two sticks.

The B-scan images with synthetic and experimental data are shown in Figures 10(a) and 10(b), respectively. The final inversion images based on the Kirchhoff migration are illustrated in Figures 11(a) and 11(b), respectively.

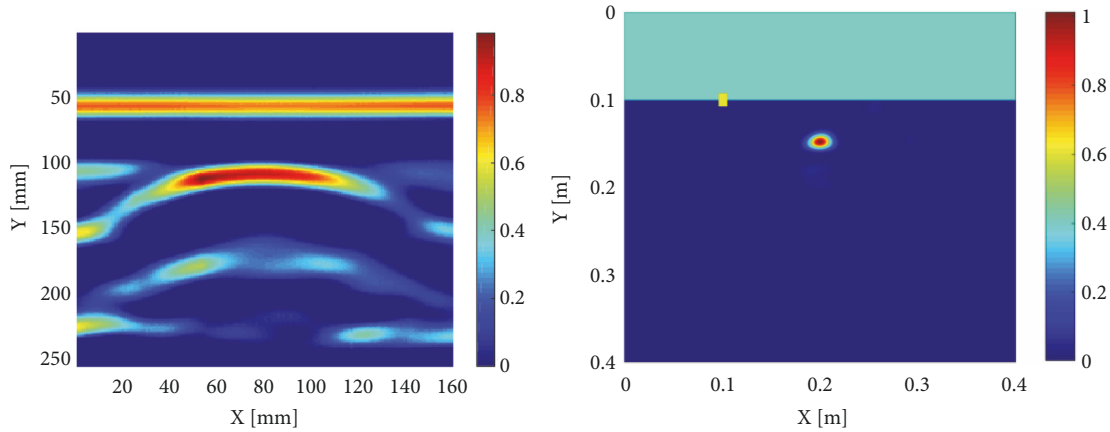

(a) B-scan image (b) Imaging by using the Kirchhoff migration

Figure 8: Imaging with experimental data.

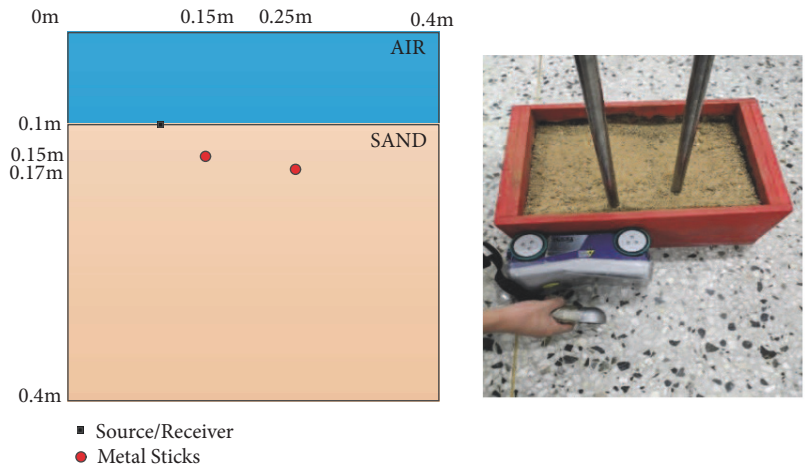

(a) Locations of the first transmitter/receiver and the two small targets (b) Experiment site

Figure 9: Locating two small scatterers buried in sand.

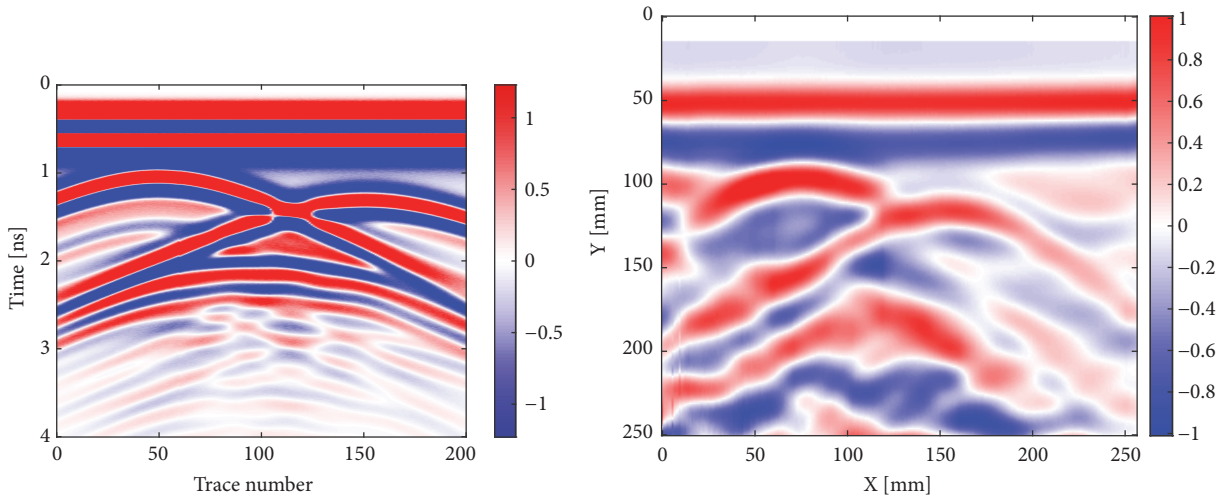

(a) Synthetic data at the noise level 20% (b) Experimental data

Figure 10: Comparison of the B-scan images with the synthetic data at noise level 20% (a) and experimental data (b).

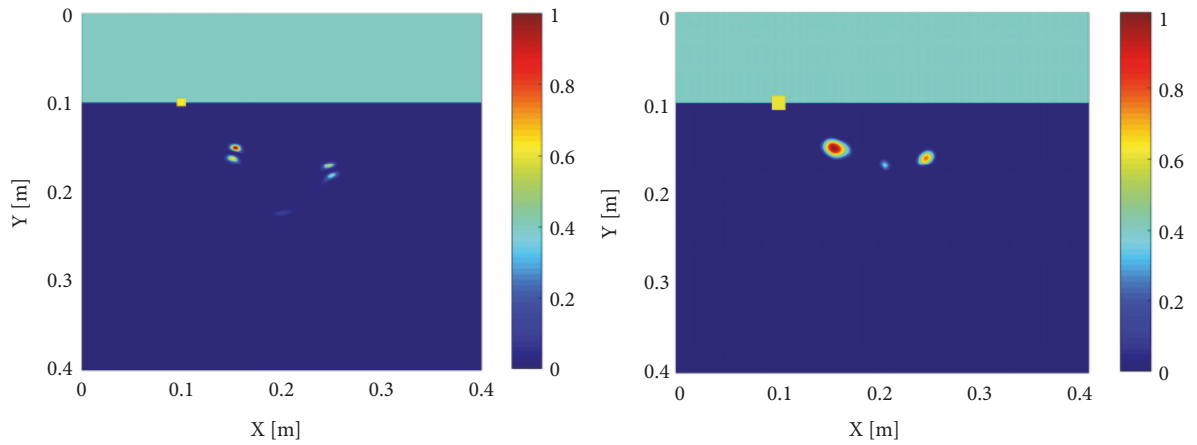

(a) Synthetic data at the noise level 20%

(b) Experimental data

Figure 11: Comparison of the images formed by the Kirchhoff migration scheme.

As shown in Figure 10, the B-scan results in both simulation and experiment can indicate a local peak in the position of the metal sticks, verifying the correctness of the inversion scheme. In Figure 11, the local maximum values of the indicator function are obtained approximately at (0.15, 0.15) and (0.25, 0.17), which agree well with the positions of the targets in our model. From the experiment image, it can be concluded that the contour image and the position of the left metal stick agree well with the true scatterers, but the size of the right one is not well reconstructed. Further, there is an untrustworthy imaging area between the two metal sticks, maybe due to the offset of the two maximizes nearby.

4. Imaging Extended Scatterers

The main purpose of this section is to test the Kirchhoff migration for imaging extended scatterers from synthetic data of several incident electric dipoles. As in the previous section, the forward data are obtained by the software GprMax. We consider the second case of our inverse electromagnetic scattering problem formulated at the end of Section 2, where the source positions are uniformly distributed on the circle $|x-O| = R$ for some $R > 0$, where $O = (o_1, o_2) \in \mathbb{R}^2$. Denote by $M > 0$ the number of incident dipoles. The Cartesian coordinates of the m-th dipole can be formulated as

$$y^{(m)} = O + R\left(\cos\theta_m, \sin\theta_m\right),$$
$$\theta_m := \frac{2m\pi}{M}, \quad m = 1, 2, \ldots, M. \tag{17}$$

In all examples we use $N = 16$ receivers $x^{(n)}$ $(n = 1, 2, \ldots, 16)$ equally spaced on $|x - O| = R$. For notational convenience, we use $u^s_{n,m}(t) = u^s_{n,m}(x^{(m)}, t; x^{(n)})$ to represent the scattered signal excited by the n-th transmitter recorded at the m-th receiver. The flight time of an impulsive signal from $y^{(n)}$ to a sampling point $z = (z_1, z_2)$ and then back to $x^{(m)}$ is then given by

$$t_{n,m}(z) = \frac{\left|y^{(n)} - z\right| + \left|z - x^{(m)}\right|}{c}, \quad n, m = 1, 2, \ldots, 16. \tag{18}$$

In this case the imaging function based on Kirchhoff migration scheme can be formulated as

$$I(z) = \left|\sum_{n=1}^{N}\sum_{m=1}^{M} u^s_{n,m}\left(t_{n,m}(z)\right)\right|^2 > 0. \tag{19}$$

In all of our numerical examples to be reported below, we set $O = (0.35, 0.35)$. The sampling region is set to be the rectangular domain $(0, 0.7) \times (0, 0.7)$. The homogeneous background medium is set to be air, with the dielectric constant $\varepsilon = 1$ and the electric conductivity $\sigma = 0$. Unless otherwise stated, the excitation frequency of a Ricker wave is taken as $f = 10$GHz. The amplitude is set to be $A = 1$ and the time window is $T = 4$ns.

In the first example, we excite only one electric dipole located at $y^{(4)}$ and measure the scattered field at $x^{(n)}$ for $n = 1, 2, \ldots, 16$. Three types of scatterers will be recovered: two small circular metals, a square-like metal, and an L-shaped metal; see Figures 12(a), 12(c), and 12(e). The last two targets will be referred to as extended scatterers, since their size is much bigger than the incident wavelength. The circular metals are centered at A(0.25, 0.35) and B(0.45, 0.35) with the radius 0.01 m. They can be treated as point-like scatterers, because their radiuses are both much smaller than the wavelength $\lambda = 0.3$m corresponding to $f = 10$GHz. The coordinates of the corners of the square-like metal are given by A(0.275, 0.425), B(0.425, 0.425), C(0.425, 0.275), and B(0.275, 0.275), and those for the L-shaped metal are A(0.275, 0.475), B(0.35, 0.475), C(0.35, 0.35), D(0.475, 0.35), E(0.475, 0.275), and F(0.275, 0.275). Figures 12(b), 12(d), and 12(f) show the reconstructions from the data of one dipole only. It can be seen that a single source can be used to capture the position of point scatterers and the illuminated boundary

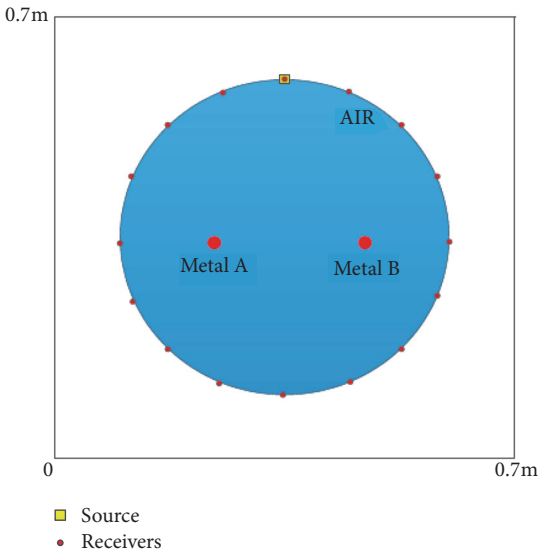

(a) Two small objects

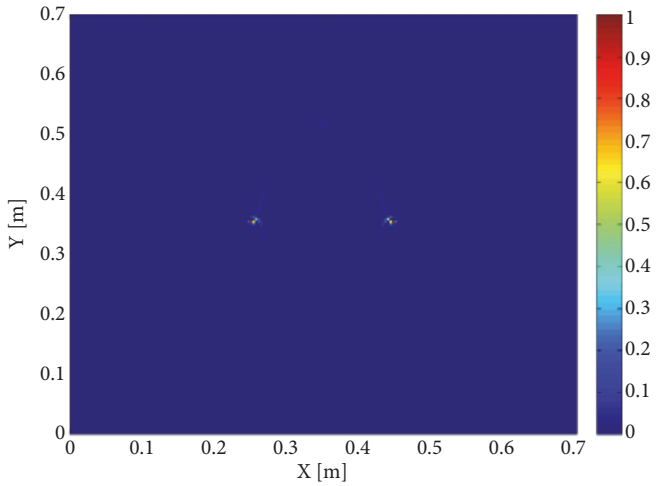

(b) Location of the two small objects

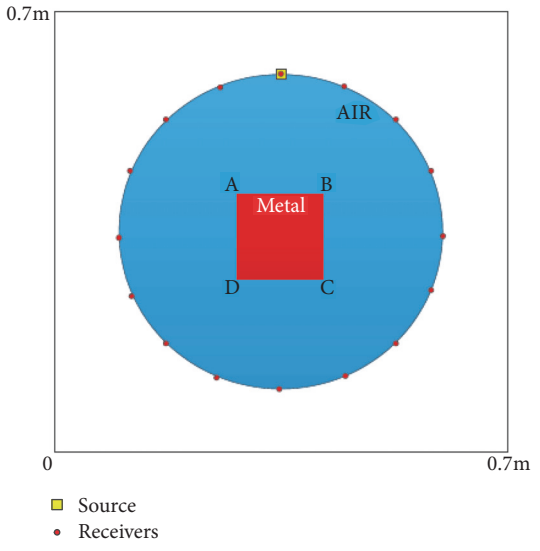

(c) A square-like metal

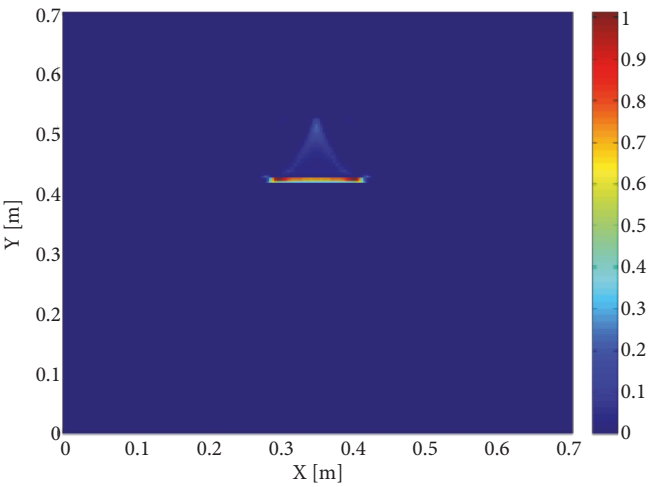

(d) Imaging of the square-like metal

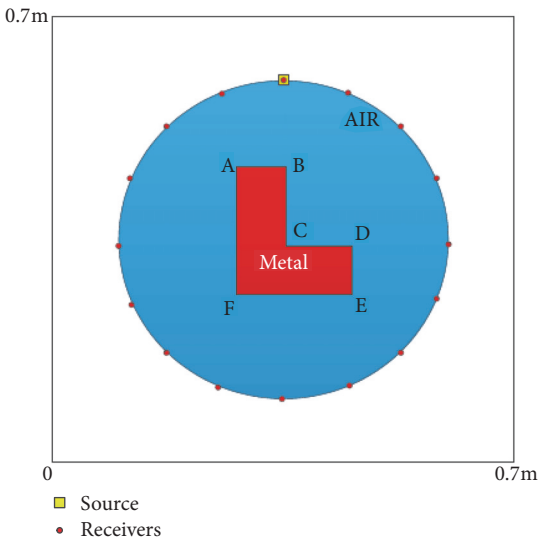

(e) An L-shaped metal

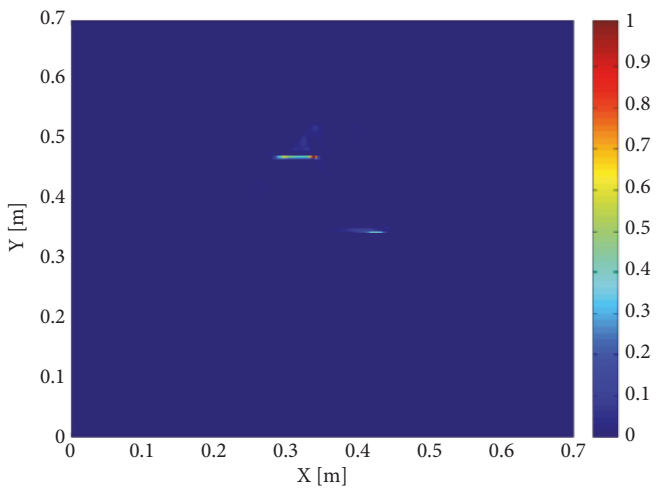

(f) Imaging of the L-shaped metal

Figure 12: Imaging small and extended metals with a single incoming dipole.

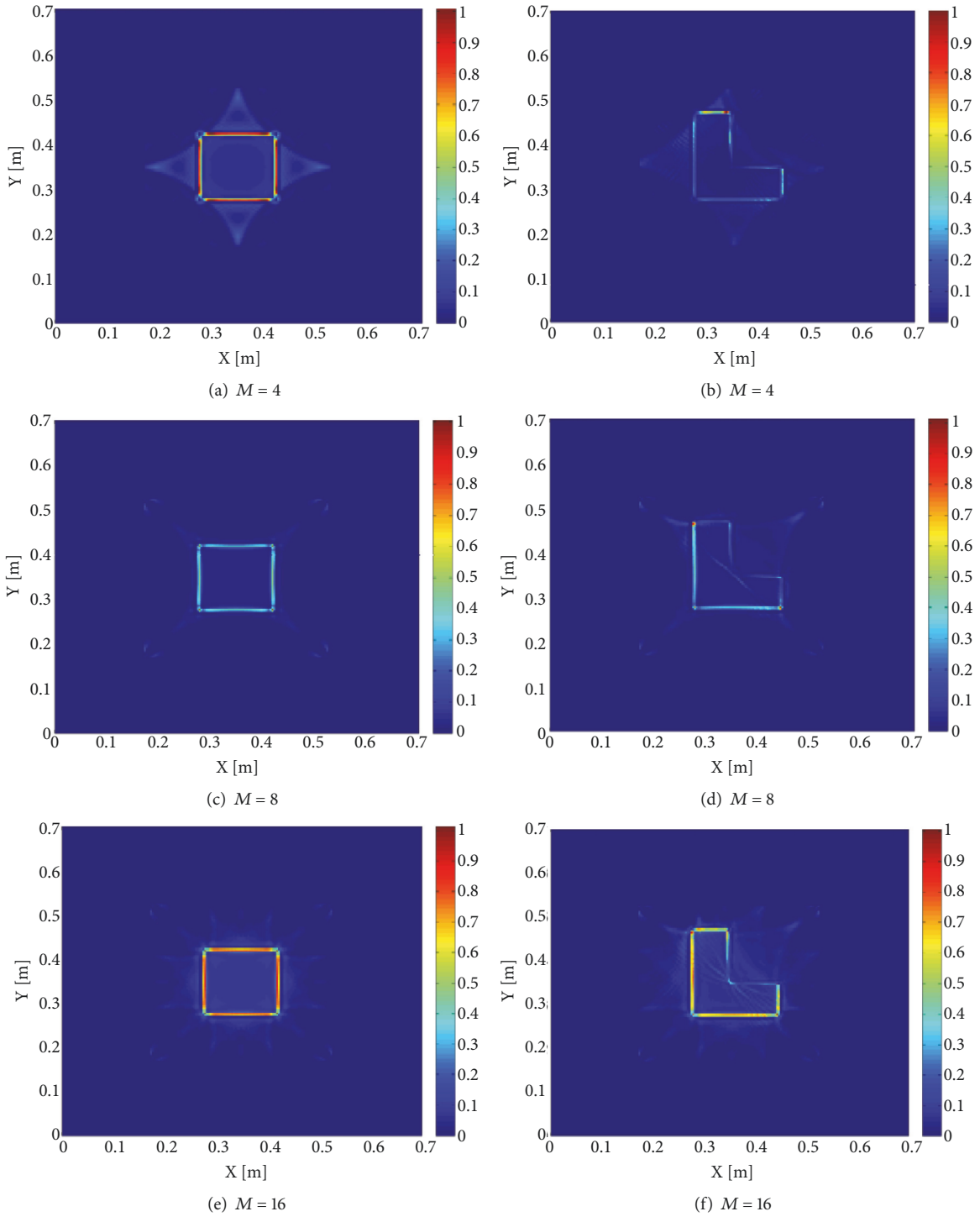

FIGURE 13: Imaging a square-like object (left) and an L-shape object (right) by M transmitters and $N = 16$ receivers.

of the square-like and L-shaped scatterers. However, the entire shape of extended objects cannot be well reconstructed.

In the second example, we increase the number of incident dipoles for reconstructing the entire shape; see Figure 13. The data of four incident waves without noise can generally produce a full-range image of an extended scatterer. However, there are bigger background disturbances and the scatterer cannot be accurately recovered. Using eight and sixteen incoming sources can image the outline of the scatterer. In Figures 13(e) and 13(f), the maximum values of the indicator are almost distributed on the contour of the object and the imaging is better than the case of eight dipoles. This means that sixteen sources are capable of imaging the scatterer, and therefore it is not necessary to use additional

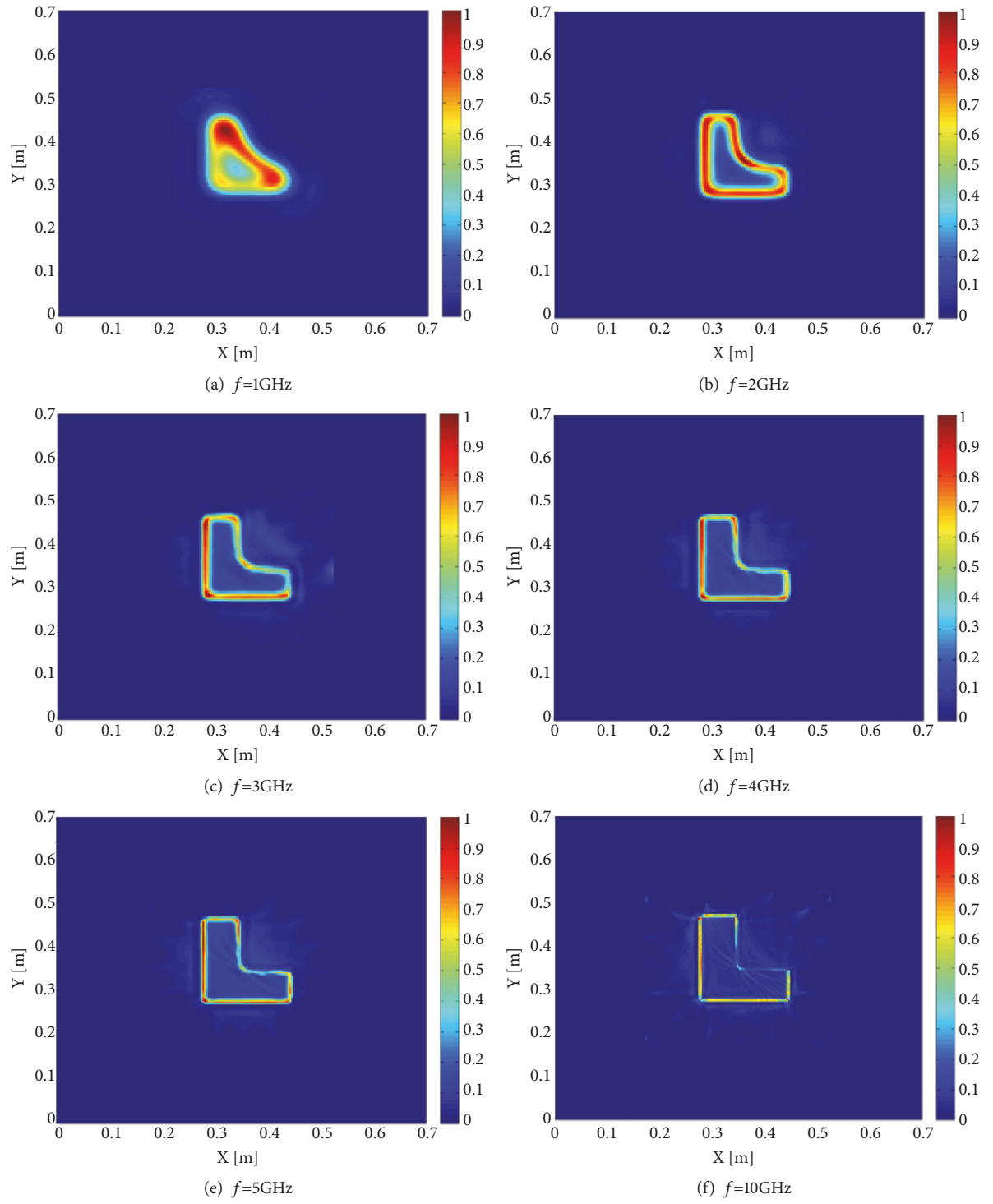

FIGURE 14: Imaging an L-shape object by M=16 transmitters and N=64 receivers (f is the excitation frequency of the sources).

sources. Hence, the data of multiple point sources in different directions need to be measured in order to better capture the shape of the target.

In the third example, we discuss the sensitivity of the imaging quality to the center frequency of incident pulse functions. We use M=16 incident dipoles and N=64 receivers. As shown in Figure 14, the shape of an extended object can be imaged at various frequencies from 1GHz to 10GHz. However, at lower frequencies the target cannot be accurately recovered. Increasing the excitation frequency of the source (which means a shorter wavelength) may lead to an image with higher resolutions.

5. Conclusions

We apply the Kirchhoff migration approach to solve inverse scattering problems for time-dependent electromagnetic waves. The inversion scheme involves only integral calculations and is robust to polluted data at high noisy levels. We use both synthetic and experimental data to examine the performance of such a direct sampling scheme for locating point-like scatterers. The multiple-input-multiple-out scheme is used for imaging extended scatterers from the data generated by the software GprMax. Our experiments show that the data of one electric dipole can correctly reconstruct the location of two small scatterers, and that sixteen incoming sources can perfectly reconstruct the shape of an extended target. In addition, the source irradiated at 10GHz can be used to more clearly reconstruct the geometrical shape than the data of lower frequencies ranging from 1GHz to 5GHz. Our future work consists of imaging extended obstacles from experimental data buried in a random background medium, which is more challenging than the problem in a stationary homogeneous medium.

Data Availability

The data used to support the findings of this study are included within the supplementary information files.

Conflicts of Interest

The authors declare that there are no conflicts of interest regarding the publication of this paper.

Acknowledgments

The work of Hongwei Zhou and Ling Ma was supported by the National Key Research and Development Program (Grant No. 2017YFD0600101), the Fundamental Research Funds for the Central Universities (Grant No. 2572019BF08), the China Postdoctoral Science Foundation (Grant No. 2018M640288), and the Heilongjiang Postdoctoral Fund (Grant No. LBH-Z18004). The work of Guanghui Hu is supported by NSFC (Grant No. 11671028) and NSAF (Grant No. U1530401).

Supplementary Materials

We used the GSSI Mini HR hand-held ground-penetrating radar to scan the sand box in Figure 7. The ground-penetrating radar had a transmitting antenna and a receiving antenna, the transmitting antenna transmitted a Ricker wavelet excited at the frequency 2.6GHz with the amplitude 1, and the receiving antenna received data as in the supplementary information files of "data of fig7.CSV" and "data of fig9b". The difference between "data of fig7.CSV" and "data of fig9b" is that the file "data of fig7.CSV" is for one metal stick, and the file "data of fig9b" is for two metal sticks. *(Supplementary Materials)*

References

[1] J. C. Bolomey, D. Lesselier, C. Pichot, and W. Tabbara, "Physically motivated approximations in some inverse scattering problems," *Radio Science*, vol. 17, no. 6, pp. 1567–1578, 2016.

[2] V. K. Chillara and C. J. Lissenden, "Review of nonlinear ultrasonic guided wave nondestructive evaluation: theory, numerics, and experiments," *Optical Engineering*, vol. 55, no. 1, Article ID 011002, 2015.

[3] P. Lobel, R. E. Kleinman, C. Pichot, L. Blanc-Féraud, and M. Borlaud, "Conjugate-gradient method for solving inverse scattering with experimental data," *IEEE Antennas and Propagation Magazine*, vol. 38, p. 35, 1996.

[4] G. Oliveri, M. Salucci, N. Anselmi, and A. Massa, "Compressive sensing as applied to inverse problems for imaging: theory, applications, current trends, and open challenges," *IEEE Antennas and Propagation Magazine*, vol. 59, no. 5, pp. 34–46, 2017.

[5] R. Persico, "On the role of measurement configuration in contactless GPR data processing by means of linear inverse scattering," *IEEE Transactions on Antennas and Propagation*, vol. 54, no. 7, pp. 2062–2071, 2006.

[6] A. Kirsch and R. Kress, "On an integral equation of the first kind in inverse acoustic scattering," in *Inverse Problems*, J. R. Cannon and U. Hornung, Eds., vol. 77 of *International Series of Numerical Mathematics*, pp. 93–102, Birkhäuser Basel, 1986.

[7] A. Kirsch and R. Kress, "An optimization method in inverse acoustic scattering," in *Boundary Elements IX, Fluid Flow and Potential Applications*, C. A. Brebbia et al., Ed., vol. 3, pp. 3–18, Springer, Berlin, Germany, 1987.

[8] D. Colton and P. Monk, "A novel method for solving the inverse scattering problem for time-harmonic acoustic waves in the resonance region," *SIAM Journal on Applied Mathematics*, vol. 45, no. 6, pp. 1039–1053, 1985.

[9] D. Colton and P. Mon, "The numerical solution of the three-dimensional inverse scattering problem for time-harmonic acoustic waves," *Society for Industrial and Applied Mathematics*, vol. 8, no. 3, pp. 278–291, 1987.

[10] T. S. Angell, R. E. Kleinman, and G. F. Roach, "An inverse transmission problem for the Helmholtz equation," *Inverse Problems*, vol. 3, no. 2, pp. 149–180, 1987.

[11] M. Saqib, S. Hasnain, and D. S. Mashat, "Highly efficient computational methods for two-dimensional coupled nonlinear unsteady convection-diffusion problems," *IEEE Access*, vol. 5, pp. 7139–7148, 2017.

[12] L. Yang, J. Tian, K. Z. Rajab, and Y. Hao, "FDTD modeling of nonlinear phenomena in wave transmission through graphene," *IEEE Antennas and Wireless Propagation Letters*, vol. 17, no. 1, pp. 126–129, 2018.

[13] H. H. Gan, T. Xia, Q. I. Dai, Y. Li, and W. C. Chew, "Augmented electric-field integral equation for inhomogeneous media," *IEEE Antennas and Wireless Propagation Letters*, vol. 16, pp. 2967–2970, 2017.

[14] D. Colton and A. Kirsch, "A simple method for solving inverse scattering problems in the resonance region," *Inverse Problems*, vol. 12, no. 4, pp. 383–393, 1996.

[15] C. Bilen, A. Ozerov, and P. Pérez, "Solving time-domain audio inverse problems using nonnegative tensor factorization," *IEEE Transactions on Signal Processing*, vol. 66, no. 21, pp. 5604–5617, 2018.

[16] M. Ikehata, "Reconstruction of an obstacle from the scattering amplitude at a fixed frequency," *Inverse Problems*, vol. 14, no. 4, pp. 949–954, 1998.

[17] M. N. Akinci, M. Cayoren, and I. Akduman, "Near-field orthogonality sampling method for microwave imaging: theory and experimental verification," *IEEE Transactions on Microwave Theory and Techniques*, vol. 64, no. 8, pp. 2489–2501, 2016.

[18] G. Bao, P. Li, J. Lin, and F. Triki, "Inverse scattering problems with multi-frequencies," *Inverse Problems*, vol. 31, no. 9, Article ID 093001, 2015.

[19] G. Bao, J. Lin, and F. Triki, "A multi-frequency inverse source problem," *Journal of Differential Equations*, vol. 249, no. 12, pp. 3443–3465, 2010.

[20] G. Bao and P. Li, "Inverse medium scattering problems in near-field optics," *Journal of Computational Mathematics*, vol. 25, no. 3, pp. 252–265, 2007.

[21] G. Bao and F. Triki, "Reconstruction of a defect in an open waveguide," *Science China Mathematics*, vol. 56, no. 12, pp. 2539–2548, 2013.

[22] H. Wang and J. Liu, "On the reconstruction of Dirichlet-to-Neumann map in inverse scattering problems with stability estimates," *Science China Mathematics*, vol. 53, no. 8, pp. 2069–2084, 2010.

[23] M. Sheikholeslami, H. Keramati, A. Shafee, Z. Li, O. A. Alawad, and I. Tlili, "Nanofluid MHD forced convection heat transfer around the elliptic obstacle inside a permeable lid drive 3D enclosure considering lattice Boltzmann method," *Physica A: Statistical Mechanics and its Applications*, vol. 523, pp. 87–104, 2019.

[24] M. Fink, "Time reversed acoustics," *Physics Today*, vol. 50, no. 3, pp. 34–40, 1997.

[25] E. Baysal, D. D. Kosloff, and J. W. C. Sherwood, "Reverse time migration," *Geophysics*, vol. 48, no. 11, pp. 1514–1524, 1983.

[26] L. Oksanen, "Solving an inverse obstacle problem for the wave equation by using the boundary control method," *Inverse Problems*, vol. 29, no. 3, pp. 35004–35015, 2013.

[27] D. Russell Luke and R. Potthast, "The point source method for inverse scattering in the time domain," *Mathematical Methods in the Applied Sciences*, vol. 29, no. 13, pp. 1501–1521, 2006.

[28] M. Ikehata, "Extracting the geometry of an obstacle and a zeroth-order coefficient of a boundary condition via the enclosure method using a single reflected wave over a finite time interval," *Inverse Problems*, vol. 30, no. 4, Article ID 045011, 2014.

[29] B. W. Drinkwater and P. D. Wilcox, "Ultrasonic array for non-destructive evaluation: a review," *NDT & E International*, vol. 39, no. 7, pp. 525–541, 2006.

[30] C. Holmes, B. W. Drinkwater, and P. D. Wilcox, "Post-processing of the full matrix of ultrasonic transmit-receive array data for non-destructive evaluation," *NDT & E International*, vol. 38, no. 8, pp. 701–711, 2005.

[31] Y. Guo, D. Hömberg, G. Hu, J. Li, and H. Liu, "A time domain sampling method for inverse acoustic scattering problems," *Journal of Computational Physics*, vol. 314, pp. 647–660, 2016.

[32] V. Metelka, L. Baratoux, M. W. Jessell, A. Barth, J. Ježek, and S. Naba, "Automated regolith landform mapping using airborne geophysics and remote sensing data, Burkina Faso, West Africa," *Remote Sensing of Environment*, vol. 204, pp. 964–978, 2018.

[33] I. Catapano, A. Affinito, A. Del Moro, G. Alli, and F. Soldovieri, "Forward-looking ground-penetrating radar via a linear inverse scattering approach," *IEEE Transactions on Geoscience and Remote Sensing*, vol. 53, no. 10, pp. 5624–5633, 2015.

[34] L. Langhammer, L. Rabenstein, A. Bauder, and H. Maurer, "Ground-penetrating radar antenna orientation effects on temperate mountain glaciers," *Geophysics*, vol. 82, no. 3, pp. H15–H24, 2017.

[35] M. Zhong and J. Liu, "On the reconstruction of media inhomogeneity by inverse wave scattering model," *Science China Mathematics*, vol. 60, no. 10, pp. 1825–1836, 2017.

[36] A. Giannopoulos, "Modelling ground penetrating radar by GprMax," *Construction and Building Materials*, vol. 19, no. 10, pp. 755–762, 2005.

[37] M. Berk, C. Loo, C. G. Davey, and B. H. Harvey, "Ketamine and rapidly acting antidepressants: breaking the speed of sound or light?" *Australian & New Zealand Journal of Psychiatry*, vol. 52, no. 11, pp. 1026–1029, 2018.

[38] C. Warren, A. Giannopoulos, and I. Giannakis, "gprMax: Open source software to simulate electromagnetic wave propagation for ground penetrating radar," *Computer Physics Communications*, vol. 209, pp. 163–170, 2016.